Article

Linear Quadratic Regulator Optimal Control with Integral Action (LQRIC) for *LC*-Coupling Hybrid Active Power Filter

Qian-Rong Hong [1,2,3], Pak-Ian Chan [1,2,3], Wai-Kit Sou [1,2,3], Cheng Gong [1,2,3] and Chi-Seng Lam [1,2,3,*]

1   State Key Laboratory of Analog and Mixed-Signal VLSI, University of Macau, Macau 999078, China
2   Institute of Microelectronics, University of Macau, Macau 999078, China
3   Department of Electrical and Computer Engineering, Faculty of Science and Technology, University of Macau, Macau 999078, China
*   Correspondence: cslam@um.edu.mo or c.s.lam@ieee.org

Abstract: Renewable energy generation and nonlinear load devices will generate harmonics and reactive power to power grids, resulting in current distortion and low power factors. To solve the power quality problems, the *LC*-coupling hybrid active power filter (*LC*-HAPF) is proposed, with lower DC-link voltage and lower cost compared with conventional active power filters (APFs). The *LC*-HAPF requires a controller to operate, therefore, hysteresis current control (HCC) and proportional current control (PCC) were proposed. However, they both result in significant steady-state error. Hence, linear quadratic regulator control (LQRC) with integral action (LQRIC) is proposed for the *LC*-HAPF in this paper to mitigate the steady-state error. The *d-q-0* coordinate state-space model of the LQRIC-controlled *LC*-HAPF is derived, and a detailed design guideline of the weighting matrices Q and R of LQRIC is given. By the state-space model and weighting matrices, the gain matrix K of LQRIC can be acquired by MATLAB, thus a good steady-state performance can be ensured. Finally, the simulation results of different controllers for the *LC*-HAPF under 40V and 50V DC-link voltages are given to verify the effectiveness of the proposed LQRIC. The experimental results of LQRIC-controlled *LC*-HAPF are also given to verify the feasibility of the proposed LQRIC.

Keywords: *LC*-coupling hybrid active power filter; power quality; current harmonic; linear quadratic regulator control; optimal control

1. Introduction

In recent years, clean and renewable energy, such as solar power and wind power, has been vigorously promoted and applied [1–3]. However, the photovoltaic (PV) systems [1] and typical wind power systems [2] require inverters to operate. They cause power quality issues such as a low power factor and current harmonic pollution, which result in the failure of electrical equipment, the interference of communication circuits, etc., bringing economic losses to societies [4,5].

In order to solve the power quality problem, capacitor bank (CB) was proposed and used for reactive power compensation in the 1900s. In the 1940s, passive power filter (PPF) was proposed to achieve both reactive power and harmonic compensation [6]. However, it can only compensate fixed harmonic frequency and suffers from resonance problems. Therefore, the active power filter (APF), which combines the voltage source inverter (VSI) and inductor, was proposed in 1976 [7]. It overcomes the shortcomings of CB and PPF, and can achieve dynamic compensation. However, APF has the problem of high cost due to the high DC-link voltage. The hybrid active power filter (HAPF) was proposed to overcome the disadvantages of PPF and APF. It can reduce the operation cost by reducing the DC-link voltage [8–10]. There are different topologies of HAPF. Among them, the *LC*-coupling hybrid active power filter (*LC*-HAPF), which has an *LC* branch and a voltage source inverter (VSI) in series, was proposed in 2003. It can achieve harmonic current and reactive power

compensation [8–11]. The thyristor-controlled *LC*-coupling hybrid active power filter (TC*LC*-HAPF) was proposed in 2014 [12], and can provide a wide range of reactive power compensation for both capacitive and inductive loads in the medium-voltage-level power system. However, it also increases the control complexity and power consumption. Next, *LCLC*-coupling hybrid active power filter (*LCLC*-HAPF) was proposed in 2020 [13]. It has a good high-order harmonic attenuation characteristic and lower inductor cost. However, it has stability problems and needs the assistance of active damping control. Therefore, considering the complexity and the system stability, the *LC*-HAPF is mainly focused on in this paper.

In addition to the topology of the *LC*-HAPF, the controller design also plays an important role in the compensation performance. Hysteresis current control (HCC) is the most widely used control method and provides fast transient response and acceptable steady-state performance [14]. However, due to its varied switching frequency, it generates harmonic current in a wide frequency range, resulting in a large output current ripple. Thus, the classical fixed switching frequency control, proportional current control (PCC), is proposed [15] to mitigate the current ripple for a better current tracking ability comparing with the HCC. However, the control gain optimization of PCC requires a trial-and-error process, therefore retaining a certain degree of steady-state error.

To obtain a lower steady-state error, a linear quadratic regulator control (LQRC) [16–23] was proposed for APF, HAPF and other applications due to the good steady-state performance. Moreover, some research suggests that LQRC with integral action (LQRIC) [24–27] is able to achieve a better steady-state performance because of the integral term. Therefore, this paper proposes the LQRIC for the *LC*-HAPF to achieve superior steady-state performance, and the LQRC for the *LC*-HAPF for the comparative study. Moreover, the gain matrix K of LQRC and LQRIC is obtained from the cost function of state errors, weighting matrices and system state space model. It results in a better steady-state performance than the PCC, whose gain optimization is just the trial-and-error process.

The objective of this paper is to design a LQRIC for the *LC*-HAPF to improve the steady-state performance under low DC-link voltage. Figure 1 is the graphical abstract of this paper.
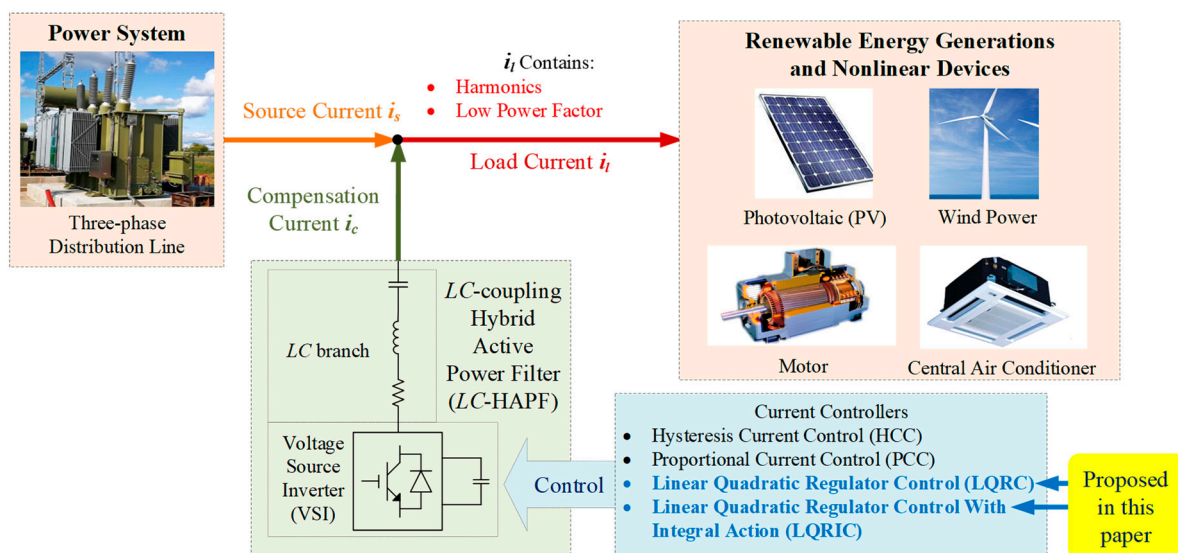
Figure 1. The graphical abstract.

The contributions of this paper are summarized as follows:

(1) A LQRIC for the three-phase four-wire *LC*-HAPF is proposed to obtain a superior compensation performance.
(2) Design the state-space model in *d-q-0* coordinate of a LQRIC-controlled *LC*-HAPF.

(3) Study the design of the weighting matrices, *Q* and *R*, of the LQRIC for *LC*-HAPF to ensure a good compensation performance.

(4) Compare the simulation results with HCC, PCC and LQRC under different DC-link voltage conditions and verify the effectiveness of the proposed LQRIC for the *LC*-HAPF.

(5) The experimental results for LQRIC under different DC-link voltages are given to verify the feasibility of the proposed LQRIC.

The arrangement of this paper is shown below. Section 2 establishes the system configuration of the three-phase four-wire *LC*-HAPF, and also gives the system model and introduces the parameter design. Then, Section 3 introduces the design of the proposed LQRC and LQRIC. The state-space model of *LC*-HAPF in *d-q-0* coordinate and the design method of the weighting matrices, Q and R, are also given. Section 4 provides the overall control block diagram of the different controllers for the *LC*-HAPF. Section 5 provides the simulation results for verifying the effectiveness of the proposed LQRIC. Section 6 provides the experimental results for verifying the feasibility of the proposed LQRIC. The overall performance of different controllers is discussed in Section 7. Finally, the paper is concluded in Section 8.

2. Circuit Configuration of *LC*-HAPF

2.1. Circuit Configuration and System Modeling

Figure 2 shows a three-phase four-wire *LC*-HAPF with a balanced nonlinear load [9–11]. The subscript *x* indicates the phase *a*, *b*, *c* and *n*. v_{sx}, i_{sx}, v_x and i_{Lx} are the source voltage, source current, the point of common coupling (PCC) voltage, and load current for each phase, respectively. i_{cx}, v_{cx} and v_{invx} are the compensation current, compensation capacitor voltage and inverter output voltage, respectively. L_{Lx}, R_{Lx} and C_{Lx} are the inductor, resistor and capacitor of the nonlinear loads, which are the full-bridge rectifier. L_{cx}, C_{cx} and R_{cx} are the inductor, capacitor and equivalent resistance of the coupling PPF. T_{1x} and T_{2x} are the trigger signals for IGBTs. The upper and lower DC-link capacitor voltage, V_{dcU} and V_{dcL}, satisfy $V_{dcU} = V_{dcL} = 0.5V_{dc}$, where V_{dc} is the DC-link voltage of VSI.
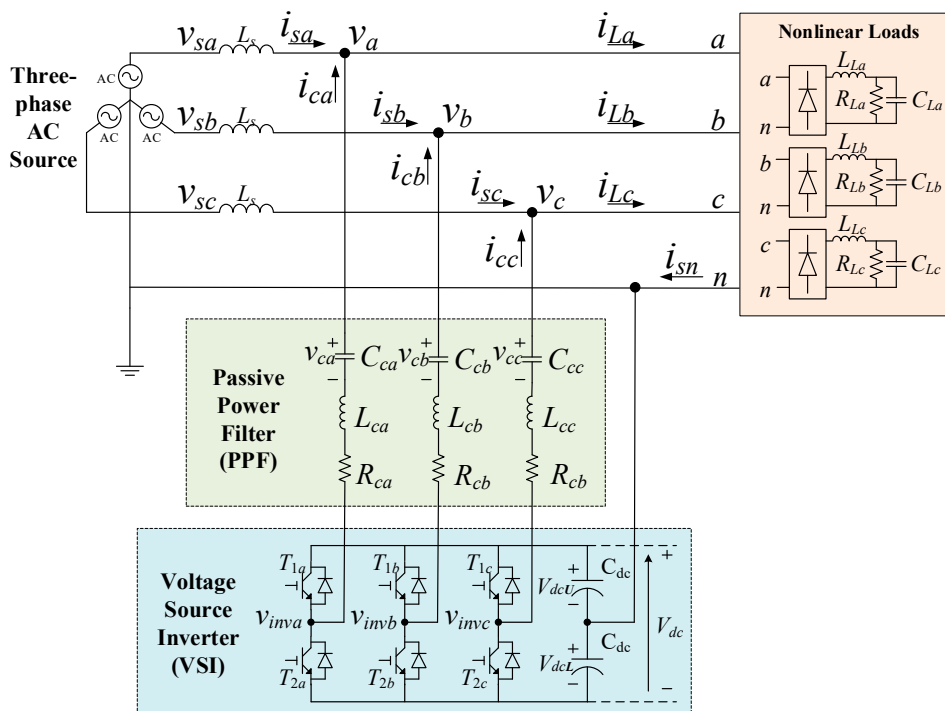
Figure 2. The circuit configuration of a three-phase four-wire *LC*-HAPF with balanced nonlinear load.

The PPF and VSI consist of *LC*-HAPF, which generate i_{cx} to compensate the grid harmonics and reactive power. The differential equations for *LC*-HAPF are set up by (1).

$$
\begin{cases}
L_{cx}\frac{di_{cx}}{dt} = v_{invx} - v_x + v_{cx} - i_{cx}R_{cx} \\
C_{cx}\frac{dv_{cx}}{dt} = i_{cx}
\end{cases}
\tag{1}
$$

Based on (1), the state-space model of *LC*-HAPF is set up by (2).

$$
\begin{cases}
\frac{d}{dt}\mathrm{e} = A\mathrm{e} + B\mathrm{u} + E\mathrm{z} \\
\mathrm{y} = C\mathrm{e} + D\mathrm{u}
\end{cases}
\tag{2}
$$

where e, u, z and y indicate state, control, disturbance and output variable matrix, and they are expressed as $\mathrm{e} = \begin{bmatrix} i_{ca} & i_{cb} & i_{cc} \end{bmatrix}^T$, $\mathrm{u} = \begin{bmatrix} v_{inva} & v_{invb} & v_{invc} \end{bmatrix}^T$, $\mathrm{z} = \begin{bmatrix} v_a - v_{ca} & v_b - v_{cb} & v_c - v_{cc} \end{bmatrix}^T$ and $\mathrm{y} = \begin{bmatrix} i_{ca} & i_{cb} & i_{cc} \end{bmatrix}^T$. T indicates the transpose of the matrix.

The upper equation in (2) is the system state differential equation of the *LC*-HAPF, the matrix A, B and E are state, control and disturbance matrix. The lower equation in (2) is the output equation of the *LC*-HAPF, which includes the output state matrix, C, and the output control matrix, D. The value of the A, B, C, D and E matrices for LQRC and LQRIC will be discussed in Section 3.

2.2. Parameter Design

The value design of L_{cx} and C_{cx} are based on the root-mean-square of PCC voltage V_{x_rms} and the reactive power for the load Q_{Lx} in (3), where X_{Cc} and X_{Lc} are the reactance of L_{cx} and C_{cx} and (4) shows the relation between L_{cx} and C_{cx}. ω_1 is the fundamental angular frequency, ω_m is the harmonic angular frequency and the subscript m is the harmonic order.

$$
\frac{V_{x\_rms}^2}{|Q_{Lx}|} = X_{Cc} - X_{Lc} = \frac{1}{\omega_1 C_{cx}} - \omega_1 L_{cx}
\tag{3}
$$

$$
L_{cx} = \frac{1}{\omega_m{}^2 C_{cx}}
\tag{4}
$$

The full-bridge rectifier load will generate odd order ($m = 3, 5, 7, \dots$) harmonic. As the main harmonic current of full bridge rectifier are the 3rd and 5th orders [28,29], in this paper, the 5th order harmonic is chosen to reduce the structure size and cost.

3. Proposed LQRC and LQRIC for *LC*-HAPF

3.1. Linear Quadratic Regulator Control (LQRC) for LC-HAPF

3.1.1. State-Space Model for LQRC-Controlled LC-HAPF

Based on (4), the small-signal state-space model is proposed for the LQRC, and the detail derivation is given as follows. In order to extract the reactive power and harmonics from the three-phase power grid, the *d-q-0* synchronous rotating coordinate system is applied. Through the *a-b-c* to *d-q-0* conversion, the active power, harmonics, reactive power and three-phase unbalance convert into *d*-axis DC component, *d*-axis AC component, *q*-axis and *0*-axis, respectively. The *a-b-c* to *d-q-0* conversion is achieved by the Park transform matrix H given in (5). After the reference current calculation in the *d-q-0* coordinate, the calculated reference compensation current will convert back to an *a-b-c* coordinate by inverse Park transform H^{-1}.

$$
H = \frac{2}{3} \begin{bmatrix}
\cos(\omega_1 t) & \cos(\omega_1 t - 120°) & \cos(\omega_1 t + 120°) \\
-\sin(\omega_1 t) & -\sin(\omega_1 t - 120°) & -\sin(\omega_1 t + 120°) \\
\frac{1}{2} & \frac{1}{2} & \frac{1}{2}
\end{bmatrix}
\tag{5}
$$

where $\omega_1 t$ is the fundamental phase angle and is obtained by phase locked loop (PLL). With the help of (5), i_{cx}, v_{invx}, v_x and v_{cx} in the *d-q-0* coordinate can be obtained. They are shown as:

$$
\begin{cases}
\begin{bmatrix} i_{cd} & i_{cq} & i_{c0} \end{bmatrix}^T = H \begin{bmatrix} i_{ca} & i_{cb} & i_{cc} \end{bmatrix}^T \\
\begin{bmatrix} v_{invd} & v_{invq} & v_{inv0} \end{bmatrix}^T = H \begin{bmatrix} v_{inva} & v_{invb} & v_{invc} \end{bmatrix}^T \\
\begin{bmatrix} v_d & v_q & v_0 \end{bmatrix}^T = H \begin{bmatrix} v_a & v_b & v_c \end{bmatrix}^T \\
\begin{bmatrix} v_{cd} & v_{cq} & v_{c0} \end{bmatrix}^T = H \begin{bmatrix} v_{ca} & v_{cb} & v_{cc} \end{bmatrix}^T
\end{cases}
\tag{6}
$$

From (1), (2), (5) and (6), the state differential equations for the *LC*-HAPF in *d-q-0* coordinate are given by (7), and the outputs of the *LC*-HAPF in the *d-q-0* coordinate are given by (8).

$$
\begin{cases}
\frac{di_{cd}}{dt} = -\frac{R_{cx}}{L_{cx}} i_{cd} + \omega_1 i_{cq} + \frac{1}{L_{cx}} v_{invd} - \frac{1}{L_{cx}} (v_d - v_{cd}) \\
\frac{di_{cq}}{dt} = -\omega_1 i_{cd} - \frac{R_{cx}}{L_{cx}} i_{cq} + \frac{1}{L_{cx}} v_{invq} - \frac{1}{L_{cx}} (v_q - v_{cq}) \\
\frac{di_{c0}}{dt} = -\frac{R_{cx}}{L_{cx}} i_{c0} + \frac{1}{L_{cx}} v_{inv0} - \frac{1}{L_{cx}} (v_0 - v_{c0})
\end{cases}
\tag{7}
$$

$$
\begin{cases}
y_d = i_{cd} \\
y_q = i_{cd} \\
y_0 = i_{c0}
\end{cases}
\tag{8}
$$

For the steady state system in (7), overlaying perturbations $\tilde{i}_{ch}$, $\tilde{v}_{invh}$, $\tilde{v}_h$ and $\tilde{v}_{ch}$ are given by (9), where the subscript *h* indicates the phase *d*, *q* and 0. [16] and the '~' denotes the perturbation value.

$$
\begin{cases}
i_{ch} = I_{ch} + \tilde{i}_{ch}, \\
v_{invh} = V_{invh} + \tilde{v}_{invh}, \\
v_h = V_h + \tilde{v}_h, \\
v_{ch} = V_{ch} + \tilde{v}_{ch}.
\end{cases}
\tag{9}
$$

where I_{ch}, V_{invh}, V_h and V_{ch} are the steady state values of compensation current, inverter voltage, PCC voltage and compensation capacitor voltage.

Based on (7)–(9), the small-signal state-space model of the *LC*-HAPF with LQRC-controlled is then set up and shown in (10).

$$
\begin{cases}
\frac{d}{dt} \tilde{e} = A\tilde{e} + B\tilde{u} + E\tilde{z} \\
\tilde{y} = C\tilde{e} + D\tilde{u}
\end{cases}
\tag{10}
$$

where $\tilde{e}$, $\tilde{u}$, $\tilde{z}$ and $\tilde{y}$ are expressed as $\tilde{e} = \begin{bmatrix} \tilde{i}_{cd} & \tilde{i}_{cq} & \tilde{i}_{c0} \end{bmatrix}^T$, $\tilde{u} = \begin{bmatrix} \tilde{v}_{invd} & \tilde{v}_{invq} & \tilde{v}_{inv0} \end{bmatrix}^T$, $\tilde{z} = \begin{bmatrix} \tilde{v}_d - \tilde{v}_{cd} & \tilde{v}_q - \tilde{v}_{cq} & \tilde{v}_0 - \tilde{v}_{c0} \end{bmatrix}^T$ and $\tilde{y} = \begin{bmatrix} \tilde{i}_{cd} & \tilde{i}_{cq} & \tilde{i}_{c0} \end{bmatrix}^T$. The matrices A, B, C, D and E are expressed as:

$$
A = \begin{bmatrix} -\frac{R_{cx}}{L_{cx}} & \omega_1 & 0 \\ -\omega_1 & -\frac{R_{cx}}{L_{cx}} & 0 \\ 0 & 0 & -\frac{R_{cx}}{L_{cx}} \end{bmatrix}, \quad
B = \begin{bmatrix} \frac{1}{L_{cx}} & 0 & 0 \\ 0 & \frac{1}{L_{cx}} & 0 \\ 0 & 0 & \frac{1}{L_{cx}} \end{bmatrix},
$$

$$
C = \begin{bmatrix} 1 & 0 & 0 \\ 0 & 1 & 0 \\ 0 & 0 & 1 \end{bmatrix}, \quad D = 0, \quad
E = - \begin{bmatrix} \frac{1}{L_{cx}} & 0 & 0 \\ 0 & \frac{1}{L_{cx}} & 0 \\ 0 & 0 & \frac{1}{L_{cx}} \end{bmatrix}.
$$

So far, the small-signal state-space model of the LQRC-controlled *LC*-HAPF is established for the derivation process of the LQRC for the *LC*-HAPF. And it applies in the following section.

3.1.2. LQRC for LC-HAPF

The objective of optimal control is to find a control system under the given constraint conditions so as to minimize the cost function, J. LQRC, which is an optimal control, has good tracking control ability, and calculates the gain by the cost function, weighting matrices and state-space model. Generally, LQRC takes the minimum value of the cost function (11) in time interval $[t_0, t_f]$ [17], where t_0 and t_f represent the initial time and final time, respectively.

$$J = \int_{t_0}^{t_f} \left(\mathbf{e}^T Q \mathbf{e} + \mathbf{u}^T R \mathbf{u} \right) dt \tag{11}$$

Q is a state weighting matrix, which is defined as a diagonal semi-positive matrix ($Q \geq 0$), and measures the importance of each phase state variable for the LQRC. R is an input weighting matrix, which is diagonal positive definite ($R > 0$) and measures the importance level of each phase control variable. They are given by (12) and (13).

$$Q = \begin{bmatrix} q_{q1} & 0 & 0 \\ 0 & q_{q2} & 0 \\ 0 & 0 & q_{q3} \end{bmatrix} \tag{12}$$

$$R = \begin{bmatrix} r_{q1} & 0 & 0 \\ 0 & r_{q2} & 0 \\ 0 & 0 & r_{q3} \end{bmatrix} \tag{13}$$

when e and u indicate the error and input, q_{qi} ($i = 1, 2, 3, \dots$) represents the weighting value of corresponding e, and r_{qi} represents the weighting value of corresponding u. The larger value of q_{qi} means take more effect on corresponding state variable in certain phase, so as r_{qi}.

The physical meaning of minimizing the cost function (11) is to minimize the tracking error and control cost (DC-link voltage of the inverter) by minimizing the corresponding terms $\mathbf{e}^T Q \mathbf{e}$ and $\mathbf{u}^T R \mathbf{u}$.

To solve the optimal control problem for this dynamical system, the Hamiltonian function F with Lagrange multipliers λ in (14) is constructed.

$$F[\mathbf{e}, \mathbf{u}, \lambda, t] = \frac{1}{2} \left[\mathbf{e}^T Q \mathbf{e} + \mathbf{u}^T R \mathbf{u} \right] + \lambda^T [A\mathbf{e} + B\mathbf{u}] \tag{14}$$

Then, (15) is used to calculate the minimum value of F, i.e., the minimum value of the cost function, J.

$$\frac{\partial F}{\partial \mathbf{u}} = R\mathbf{u} + B^T \lambda = 0 \tag{15}$$

As R is positive and symmetrical, by (15), the optimal control variable solution u* is calculated by:

$$\mathbf{u}^* = -R^{-1} B^T \lambda \tag{16}$$

In order to realize feedback control, the positive-definite transformation matrix, P, is introduced to evaluate the λ.

$$\lambda = P \cdot \mathbf{e} \tag{17}$$

and the matrix P is the solution of Algebraic Riccati equation (ARE):

$$PA + A^T P - PBR^{-1}B^T P + Q = 0 \tag{18}$$

From (16) and (17), we have:

$$\mathbf{u}^* = -R^{-1} B^T P \cdot \mathbf{e} = K \cdot \mathbf{e} \tag{19}$$

$$K = R^{-1} B^T P \tag{20}$$

where K is the gain matrix for LQR optimal control. Every combination of Q and R matrices can obtain a unique solution for K, which can satisfy the minimum cost of (11).

From (19) and (20), the controlled system is expressed as:

$$\frac{d}{dt}e = Ae + Bu = (A - BK)e \tag{21}$$

and the design of Q and R matrices is based on Bryson's rule [30], which provides the reasonable weighting elements q_{qi} and r_{qi} that are shown in below:

$$\begin{cases} q_{qi} = \frac{1}{Maximum\ acceptable\ value\ of\ \left[e_i^2\right]} \\ r_{qi} = \frac{1}{Maximum\ acceptable\ value\ of\ \left[u_i^2\right]} \end{cases} \tag{22}$$

The overall design process of LQRC is shown as follows:

1. Select Q and R matrices based on Bryson's rule;
2. Substitute the A, B, Q and R matrices to (18) and obtain the P matrix;
3. Using the R, B and P matrices to obtain the optimal control gain K matrix.

3.2. LQRC with Integral Action (LQRIC) for LC-HAPF

The LQRIC adds the integral term of each state variable on the basis of LQRC, which aims to reduce the steady state error of the system. Thus, for the small-signal state-space model of LQRIC-controlled *LC*-HAPF, the state variable $\tilde{e}$ is upgraded and shown in (23), whereas the control variable $\tilde{u}$, disturbance variable $\tilde{z}$, and output variable $\tilde{y}$ of the LQRIC remain the same as the LQRC.

$$\tilde{e} = \begin{bmatrix} \tilde{i}_{cd} & \tilde{i}_{cq} & \tilde{i}_{c0} & \int \tilde{i}_{cd} & \int \tilde{i}_{cq} & \int \tilde{i}_{c0} \end{bmatrix}^T \tag{23}$$

The matrices A, B, C, D and E for the LQRIC-controlled *LC*-HAPF are modified accordingly and expressed as:

$$A = \begin{bmatrix} -\frac{R_{cx}}{L_{cx}} & \omega & 0 & 0 & 0 & 0 \\ -\omega & -\frac{R_{cx}}{L_{cx}} & 0 & 0 & 0 & 0 \\ 0 & 0 & -\frac{R_{cx}}{L_{cx}} & 0 & 0 & 0 \\ 1 & 0 & 0 & 0 & 0 & 0 \\ 0 & 1 & 0 & 0 & 0 & 0 \\ 0 & 0 & 1 & 0 & 0 & 0 \end{bmatrix}, B = \begin{bmatrix} \frac{1}{L_{cx}} & 0 & 0 \\ 0 & \frac{1}{L_{cx}} & 0 \\ 0 & 0 & \frac{1}{L_{cx}} \\ 0 & 0 & 0 \\ 0 & 0 & 0 \\ 0 & 0 & 0 \end{bmatrix},$$

$$C = \begin{bmatrix} 1 & 0 & 0 & 0 & 0 & 0 \\ 0 & 1 & 0 & 0 & 0 & 0 \\ 0 & 0 & 1 & 0 & 0 & 0 \end{bmatrix}, D = 0, E = -\begin{bmatrix} \frac{1}{L_{cx}} & 0 & 0 \\ 0 & \frac{1}{L_{cx}} & 0 \\ 0 & 0 & \frac{1}{L_{cx}} \\ 0 & 0 & 0 \\ 0 & 0 & 0 \\ 0 & 0 & 0 \end{bmatrix}.$$

For LQRIC, the R matrix remains the same as LQRC, whereas the Q matrix has three additional integral weighting elements, q_{q4}, q_{q5} and q_{q6}, which are shown below:

$$Q = \begin{bmatrix} q_{q1} & 0 & 0 & 0 & 0 & 0 \\ 0 & q_{q2} & 0 & 0 & 0 & 0 \\ 0 & 0 & q_{q3} & 0 & 0 & 0 \\ 0 & 0 & 0 & q_{q4} & 0 & 0 \\ 0 & 0 & 0 & 0 & q_{q5} & 0 \\ 0 & 0 & 0 & 0 & 0 & q_{q6} \end{bmatrix} \tag{24}$$

For the design of the Q matrix for LQRIC, the integral weighting elements are designed larger than the corresponding proportional weighting elements q_{q1}, q_{q2} and q_{q3}, i.e., $q_{q4} \geq q_{q1}$, $q_{q5} \geq q_{q2}$ and $q_{q6} \geq q_{q3}$, in order to achieve a better steady-state performance compared with the LQRC. Finally, based on the updated variable $\tilde{e}$ and matrices A, B, C, D, E, Q and R, the optimal control gain K matrix of the LQRIC can be obtained by the design process of LQRC in Section 3.1.2, and therefore the controlled system in (21) of LQRIC can be acquired.

4. Overall Control Strategy of *LC*-HAPF

Figure 3 shows the overall control block diagram of the LQRC and LQRIC for the *LC*-HAPF. Firstly, both i_{Lx} and i_{cx} are transformed into *d-q-0* coordinates by Park transformation, where the $\omega_1 t$ is obtained by the PLL. The reference compensation current in the *d*-axis i_{cd}^* is derived from the high pass filter (HPF). Then, the compensation current error ε_h is obtained by $\varepsilon_h = i_{ch} - i_{ch}{}^*$. After that, the ε_h can be transformed into $v_{invh}{}^*$ by the LQRC or LQRIC, and the $v_{invh}{}^*$ is converted back into the *a-b-c* coordinate, which is $v_{invx}{}^*$. It will be applied into the PWM so as to generate the inverter trigger signals T_{1x} and T_{2x} to control the IGBTs in the VSI of *LC*-HAPF. Finally, the VSI outputs v_{invx} to the PPF branch in Figure 1, in which i_{cx} injects into the power grid and compensates the reactive power and harmonics current.
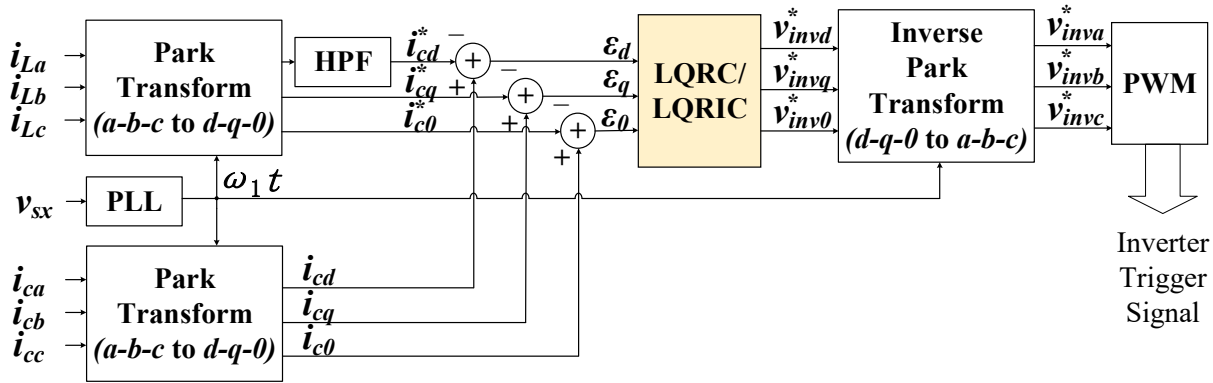
Figure 3. The overall block diagram of LQRC and LQRIC for *LC*-HAPF.

In this paper, a comparative study of the compensation for *LC*-HAPF with different controllers will be demonstrated in order to verify the effectiveness of the LQRCI for *LC*-HAPF. The HCC and PCC are applied to the *LC*-HAPF for the comparative study, and their control block diagrams and parameter designs will be mentioned in the following sections.

4.1. Hysteresis Current Control (HCC)

The control block diagram of HCC [14] is shown in Figure 4a. The HCC is derived by:

$$v_{invx} = \begin{cases} \frac{V_{dc}}{2}, & \text{for } \varepsilon_x \geq B; \\ -\frac{V_{dc}}{2}, & \text{for } \varepsilon_x \leq B. \end{cases} \tag{25}$$
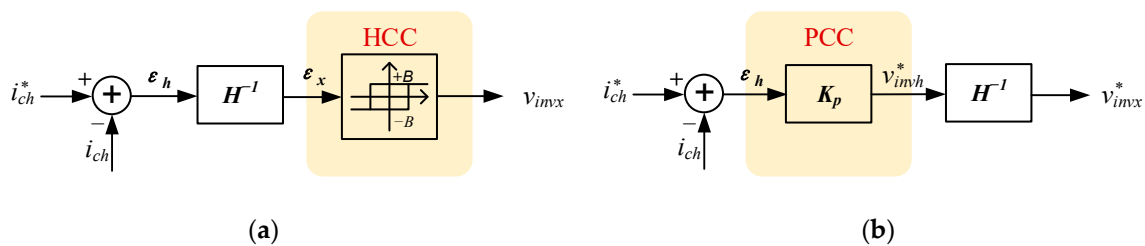
Figure 4. Control block diagram of (**a**) HCC; (**b**) PCC.

The design of the hysteresis band *B* needs to satisfy (26).

$$B = \frac{V_{dc}}{8L_{cx}f_{sw}} \tag{26}$$

where f_{sw} is the switching frequency.

4.2. Proportional Current Control (PCC)

The control block diagram of PCC [15] is shown in Figure 4b. The PCC is expressed by:

$$v_{invx}^* = K_p \varepsilon_x \tag{27}$$

where K_p is the proportional gain and the K_p can be designed by:

$$0 < K_p \leq \frac{8L_{cx}}{3T_s} \tag{28}$$

where T_s is the sampling time.

5. Simulation Result

The system parameters and control parameters of different controllers for simulation are shown in Table 1. MATLAB/Simulink is used to simulate the compensation results of the different current controllers for the three-phase four-wire *LC*-HAPF. The simulation results before and after HCC, PCC, LQRC and LQRIC-controlled *LC*-HAPF under 50 V and 40 V DC-link voltage conditions are shown in Figures 5 and 6, and the values are summarized in Tables 2 and 3.

Table 1. System parameters and control parameters of different controllers for simulation.

System Parameters	Values	Controller Parameters	Values
v_{sx}, f	110 V$_{rms}$, 50 Hz	*H* (HCC)	0.156
L_s	0.5 mH	K_p (PCC)	250
L_{Lx}, C_{Lx}, R_{Lx}	35 mH, 400 μF, 43 Ω	$q_{q1}, q_{q2}, q_{q3}, r_{q1}, r_{q2}, r_{q3}$ (LQRC)	350, 310, 370, 0.01, 0.01, 0.01
L_{cx}, C_{cx}, R_{cx}	8 mH, 50 μF, 0.03 Ω	$q_{q1}, q_{q2}, q_{q3}, q_{q4}, q_{q5}, q_{q6}, r_{q1}, r_{q2}, r_{q3}$ (LQRIC)	260, 240, 290, 830, 820, 450, 0.01, 0.01, 0.01
V_{dc}	100 V		
f_s	10 kHz		

Table 2. Simulation results before and after *LC*-HAPF compensation under 50V DC-link voltage.

	Before Compensation	After Compensation			
		HCC	PCC	LQRC	LQRIC
THD$_{isa}$ (%)	33.7	11.3	8.3	7.4	6.2
THD$_{isb}$ (%)	33.7	10.9	8.7	7.9	6.8
THD$_{isc}$ (%)	33.7	11.3	8.7	8.1	6.8
PF	0.76	0.99	1.00	1.00	1.00
Q$_{Total}$ (var)	615.1	4.2	3.8	2.8	2.1
Total SW loss (W)	/	25.0	26.3	26.6	27.0
i_{sa} (Arms)	3.28	2.50	2.48	2.47	2.46
i_{sb} (Arms)	3.28	2.50	2.47	2.47	2.46
i_{sc} (Arms)	3.28	2.49	2.48	2.47	2.46
i_{sn} (Arms)	2.97	0.49	0.44	0.41	0.38
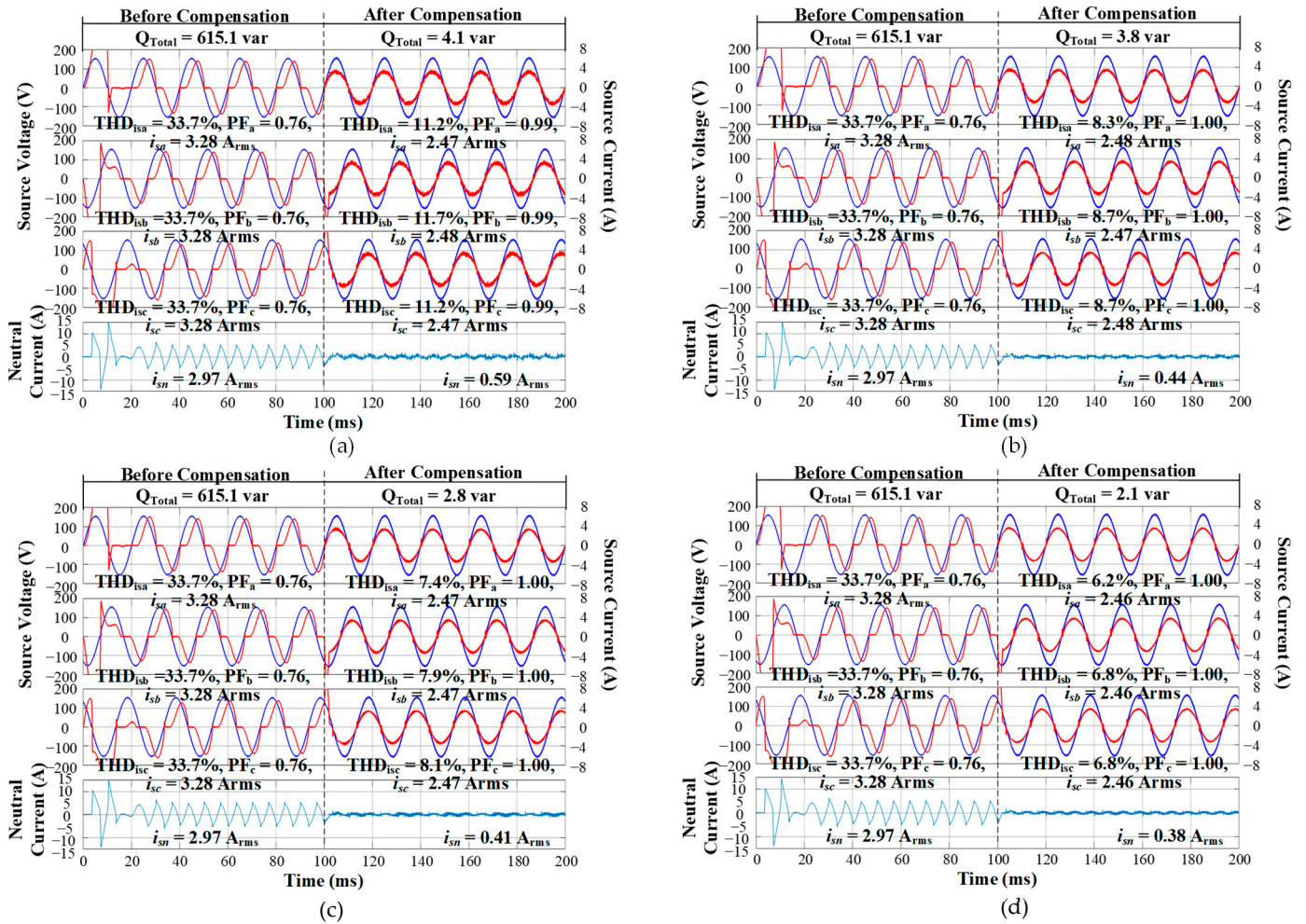
Figure 5. Simulation results of three-phase PCC voltage, source current and neutral current before and after *LC*-HAPF compensation with (**a**) HCC; (**b**) PCC; (**c**) LQRC; and (**d**) LQRIC under 50 V DC-link voltage. (For each graph, the blue lines are the waveforms of source voltage, the red lines are the waveforms of source current, and the peacock blue lines are the waveforms of neutral current.)

Table 3. Simulation results before and after the *LC*-HAPF compensation under 40V DC-link voltage.

	Before Compensation	After Compensation			
		HCC	PCC	LQRC	LQRIC
THD_{isa} (%)	33.7	15.4	14.4	8.2	6.1
THD_{isb} (%)	33.7	15.6	15.0	7.9	6.3
THD_{isc} (%)	33.7	15.9	14.3	8.0	7.1
PF	0.76	0.99	0.99	1.00	1.00
Q_{Total} (var)	615.1	10.0	9.7	3.6	2.9
Total SW loss (W)	/	12.3	13.8	15.9	15.9
i_{sa} (Arms)	3.28	2.49	2.46	2.46	2.46
i_{sb} (Arms)	3.28	2.49	2.45	2.46	2.46
i_{sc} (Arms)	3.28	2.48	2.45	2.46	2.46
i_{sn} (Arms)	2.97	0.79	0.77	0.41	0.36
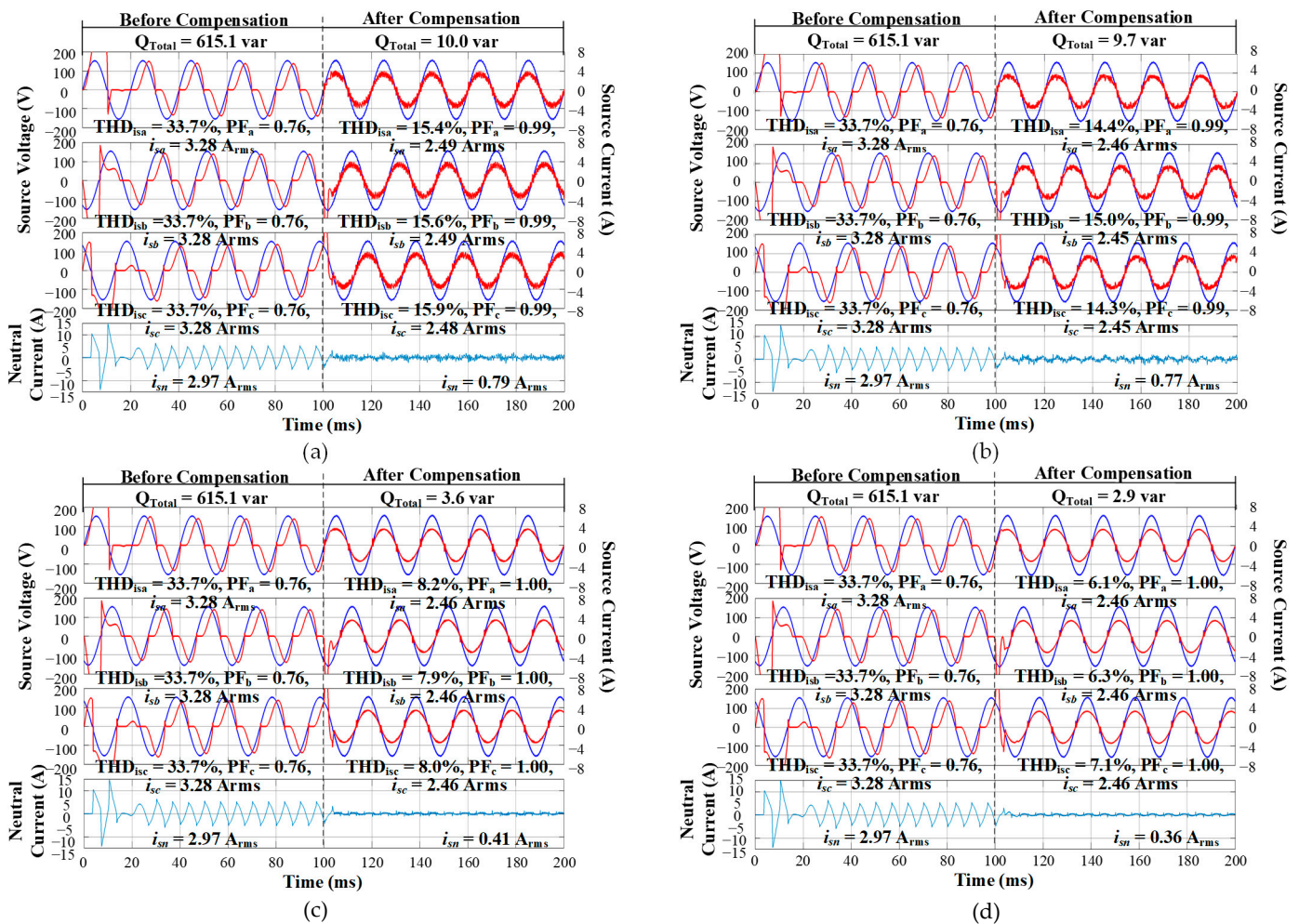
Figure 6. Simulation results of three-phase PCC voltage, source current and neutral current before and after the *LC*-HAPF compensation with (**a**) HCC; (**b**) PCC; (**c**) LQRC; and (**d**) LQRIC under 40 V DC-link voltage. (For each graph, the blue lines are the waveforms of source voltage, the red lines are the waveforms of source current, and the peacock blue lines are the waveforms of neutral current.)

5.1. Hysteresis Current Control (HCC)

After compensation, the simulation results of HCC under 50V DC-link voltage conditions are shown in Figure 5a and Table 2. The harmonic currents are compensated, and the total source current harmonic distortion (THD$_{isx}$) is reduced from 33.7% to about 11.3%. Also, the compensated i_{sn} is 0.49 Arms and the compensated i_{sx} is around 2.50 Arms. Additionally, the three-phase power factors (PFs) are the same and increase to 0.99, and the Q$_{Total}$ reduces to 4.2 var. The total switching loss (total SW loss) of HCC is 25.0 W.

The simulation results of HCC under 40V DC-link voltage conditions are shown in Figure 6a and Table 3. The THD$_{isx}$ reduces to about 15.9%. Also, the compensated i_{sn} is 0.79 Arms and the compensated i_{sx} is around 2.49 Arms. Additionally, the three-phase PFs are the same and increase to 0.99, and the Q$_{Total}$ reduces to 10.0 var. The total SW loss of HCC is 12.3 W.

5.2. Proportional Current Control (PCC)

The simulation results of the *LC*-HAPF with PCC under 50V DC-link voltage conditions are shown in Figure 5b and Table 2. The THD$_{isx}$ reduces to about 8.7% after compensation. The compensated i_{sn} is 0.44 Arms and the compensated i_{sx} is around 2.48 Arms. Moreover, the three-phase PFs are equal to 1, and the Q$_{Total}$ reduces to 3.8 var. The total SW loss of PCC is 26.3 W.

The simulation results of the *LC*-HAPF with PCC under 40V DC-link voltage conditions are shown in Figure 6b and Table 3. The THD$_{isx}$ reduces to about 15.0% after compensation. The compensated i_{sn} is 0.77 Arms and the compensated i_{sx} is around 2.45 Arms. Moreover, the three-phase PFs increase to 0.99, and the Q$_{Total}$ reduces to 9.7 var. The total SW loss of PCC is 13.8 W.

5.3. Linear Quadratic Regulator Control (LQRC)

Figure 5c and Table 2 show the simulation results of the *LC*-HAPF with LQRC under 50V DC-link voltage conditions. After compensation, the THD$_{isx}$ reduces to about 8.1%. The compensated i_{sn} is 0.41 Arms and the compensated i_{sx} is around 2.47 Arms. The three-phase PFs are equal to 1, and the Q$_{Total}$ reduces to 2.8 var. The total SW loss of LQRC is 26.6 W.

Figure 6c and Table 3 show the simulation results of the *LC*-HAPF with LQRC under 40V DC-link voltage conditions. After compensation, the THD$_{isx}$ reduces to about 8.2%. The compensated i_{sn} is 0.41 Arms and the compensated i_{sx} is around 2.46 Arms. The three-phase PFs are equal to 1, and the Q$_{Total}$ reduces to 3.6 var. The total SW loss of LQRC is 15.9 W.

5.4. Proposed LQR Control with Integral Action Control (LQRIC)

The simulation results of the *LC*-HAPF with proposed LQRIC under 50V DC-link voltage conditions are shown in Figure 5d and Table 2. After compensation, the THD$_{isx}$ reduces to about 6.8%. The compensated i_{sn} is 0.38 Arms and the compensated i_{sx} is around 2.46 Arms. The three-phase PFs are equal to 1, and the Q$_{Total}$ reduces to 2.1 var. The total SW loss of LQRC is 27.0 W.

The simulation results of the *LC*-HAPF with proposed LQRIC under 40V DC-link voltage conditions are shown in Figure 6d and Table 3. After compensation, the THD$_{isx}$ reduces to about 7.1%. The compensated i_{sn} is 0.36 Arms and the compensated i_{sx} is around 2.46 Arms. The three-phase PFs are equal to 1, and the Q$_{Total}$ reduces to 2.9 var. Hence, the proposed LQRIC can achieve the smallest steady-state error. The total SW loss of LQRC is 15.9 W.

6. Experimental Result

To verify the feasibility of proposed LQRIC, a 110 V–5 kVA three-phase four-wire *LC*-HAPF experimental prototype was constructed and is shown in Figure 7. A digital signal processor TMS320F2812 is applied and works in a 10 kHz sampling frequency. The Mitsubishi IGBT intelligent power module PM300DSA60 is used as the power switch in the VSI.
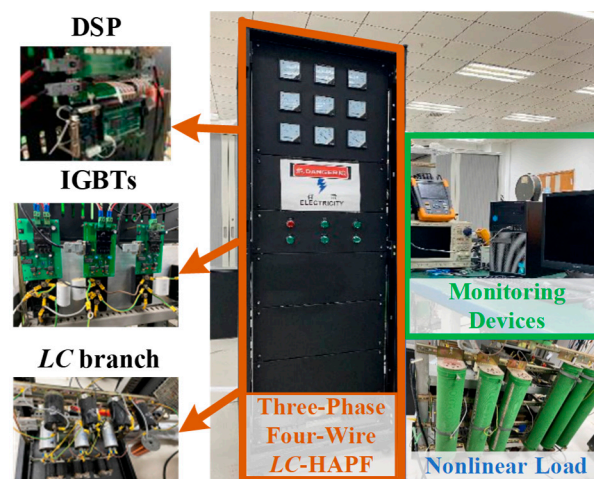
Figure 7. Experimental prototype of 110 V–5 kVA *LC*-HAPF.

This paper takes IEEE Standard 519-2014 [31] as a reference. At small experimental rated 110 V–5 kVA prototypes and I_{SC}/I_L in the range of 100 < 1000 scale, the acceptable total demand distortion (TDD) is less than or equal to 15%. Considering the worst case, the rated current is equal to the fundamental load current and results in THD = TDD $\leq$ 15%. Therefore, THD $\leq$ 15% is used as a criterion to evaluate the *LC*-HAPF current harmonic compensation performance.

The experimental results before and after the *LC*-HAPF compensation with LQRC and LQRIC under 50V and 40V DC-link voltage conditions are shown in Figures 8 and 9 and Table 4.

Table 4. Experimental results before and after the *LC*-HAPF compensation with LQRC and LQRIC.

	Before Compensation	50V DC-Link Voltage		40V DC-Link Voltage	
		LQRC	**LQRIC**	**LQRC**	**LQRIC**
THD$_{isa}$ (%)	26.2	10.1	8.8	10.7	9.2
THD$_{isb}$ (%)	26.7	9.6	8.1	10.7	8.8
THD$_{isc}$ (%)	26.2	10.0	8.8	10.6	9.1
PF	0.80	0.99	0.99	0.99	0.99
Q$_{Total}$ (var)	580	20	20	20	20
Total SW loss (W)	/	29.6	30.2	19.5	20.3
i_{sa} (Arms)	3.4	2.9	3.0	2.9	2.9
i_{sb} (Arms)	3.4	2.9	2.9	2.9	2.9
i_{sc} (Arms)	3.4	2.9	2.9	2.9	2.9
i_{sn} (Arms)	2.4	0.9	0.8	1.0	0.9

6.1. Proposed LQR Control with Integral Action Control (LQRIC)

The experimental results of LQRIC under 50V DC-link voltage conditions are shown in Figures 8c and 9c and Table 4. The THD$_{isx}$ reduces to about 8.8% after compensation. The compensated i_{sn} is 0.8 Arms and the compensated i_{sx} is around 2.9 Arms. Additionally, the three-phase PFs are the same and increase to 0.99, and the Q$_{Total}$ reduces to 20 var. The total SW loss is 30.2 W.

The experimental results of LQRIC under 40V DC-link voltage conditions are shown in Figures 8d and 9d and Table 4. The THD$_{isx}$ reduces to about 9.2% after compensation. The compensated i_{sn} is 0.9 Arms and the compensated i_{sx} is around 2.9 Arms. Moreover, the three-phase PFs are equal and increase to 0.99, and the Q$_{Total}$ reduces to 20 var. The total SW loss is 20.3 W.

6.2. Linear Quadratic Regulator Control (LQRC)

After compensation, the experimental results of LQRC under 50V DC-link voltage conditions are shown in Figures 8a and 9a and Table 4. The THD$_{isx}$ reduces to about 10.1%. Also, the compensated i_{sn} is 0.9 Arms and the compensated i_{sx} is 2.9 Arms. Additionally, the three-phase PFs are the same and increase to 0.99, and the Q$_{Total}$ reduces to 20 var. The total SW loss is 29.6 W.

The experimental results of LQRC under 40V DC-link voltage conditions are shown in Figures 8b and 9b and Table 4. The harmonic currents are compensated, and the THD$_{isx}$ reduces to about 10.7%. Also, the compensated i_{sn} is 1.0 Arms and the compensated i_{sx} is 2.9 Arms. Moreover, the three-phase PFs are equal and increase to 0.99, and the Q$_{Total}$ reduces to 20 var. The total SW loss is 19.5 W.
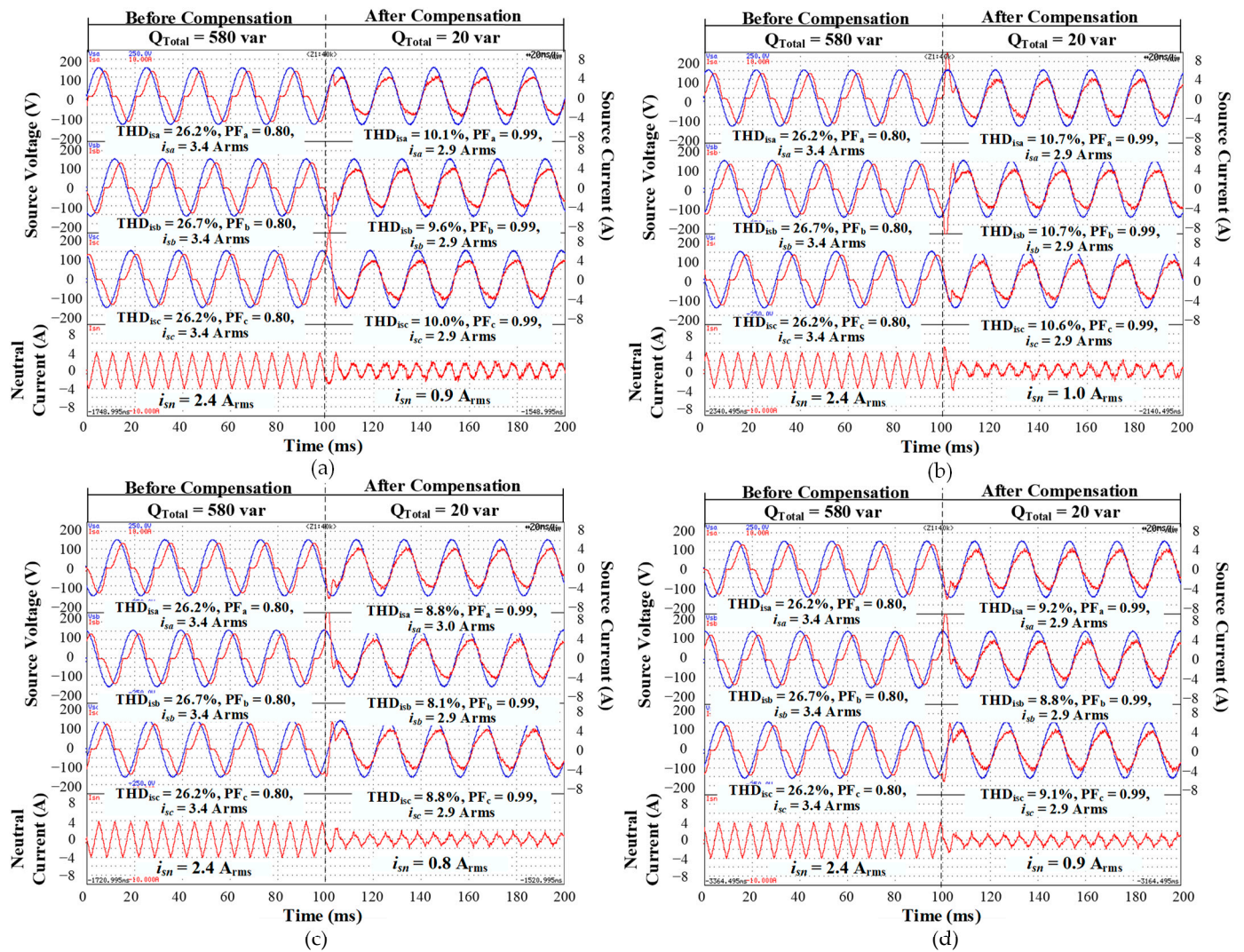
Figure 8. Experimental results of three-phase PCC voltage, source current and neutral current before and after the *LC*-HAPF compensation with (**a**) LQRC under 50V DC-link voltage; (**b**) LQRC under 40V DC-link voltage; (**c**) LQRIC under 50 V DC-link voltage and (**d**) LQRIC under 40V DC-link voltage. (For each graph, the blue lines are the waveforms of source voltage, the red lines in the 1st, 2nd and 3rd tunes are the waveforms of source current, and the red lines in last tune are the waveforms of neutral current.)
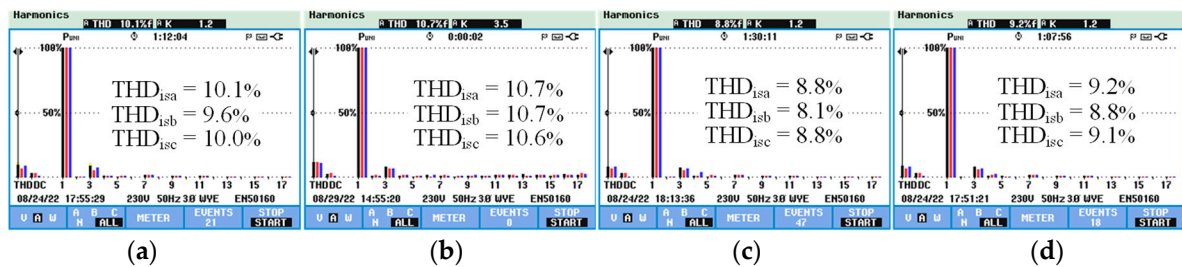
Figure 9. Experimental results of THD$_{isx}$ after the *LC*-HAPF compensation with (**a**) LQRC under 50 V DC-link voltage; (**b**) LQRC under 40V DC-link voltage; (**c**) LQRIC under 50V DC-link voltage and (**d**) LQRIC under 40V DC-link voltage.

7. Discussion

7.1. Simulation Results Comparison of Different Controllers

From the simulation results shown in Figure 5 and Table 2, all controllers can compensate the reactive power and current harmonics. Comparing four controllers, HCC shows the worst $\text{THD}i_{sx}$, the largest neutral current i_{sn} and the largest reactive power after compensation, the current after HCC compensation still exists as a large current ripple. The PCC shows a lower $\text{THD}i_{sx}$, i_{sn} and Q_{Total} than HCC with the fixed switching frequency, whereas the K_p gain of PCC is obtained by trial and error. LQRC shows a better harmonic, reactive power and neutral current compensation capability compared with PCC, as its control gain matrix K is optimized using the LQR method. LQRIC has the best harmonic and reactive power compensation capability with the lowest THD_{isx}, Q_{Total} and i_{sn} because an integral action is added to perform the error correction and the control gain K is also optimized by the LQR method.

7.2. Optimal Control of LQRC and LQRIC

From the simulation results shown in Figure 6 and Table 3, when the supplied DC-link voltage is reduced from 50V to 40V, the compensation performances of HCC and PCC become worse. A large steady-state error and reactive power exists after the HCC- and PCC-controlled *LC*-HAPF compensation, whereas the LQRC maintains a good harmonic and reactive power compensation performance. The LQRIC still shows the lowest THD_{isx}, i_{sn} and Q_{Total}, which verifies the optimal control of the proposed LQRIC.

7.3. Feasibility of LQRC and LQRIC Controllers

The experimental results in Figure 8, Figure 9 and Table 4 verify the feasibility of LQRC and LQRIC for *LC*-HAPF under 50V and 40V DC-link voltage. Followed by the IEEE standard [31], the LQRC- and LQRIC-controlled *LC*-HAPF can compensate the THD_{isx} to less than 15%, while the reactive power and neutral current are small after compensation. These results show that both LQRC and LQRIC can achieve optimal control and can compensate harmonics and reactive power even in low DC-link voltage conditions. The proposed LQRIC also shows a better steady-state and reactive power compensation performance compared with the LQRC.

8. Conclusions

In this paper, a LQRIC for the three-phase four-wire *LC*-HAPF is proposed and designed to ensure a good steady-state performance even under low DC-link voltage. The state-space model in the *d-q-0* coordinate of the LQRIC-controlled *LC*-HAPF is established and helps to obtain the reference current. The detailed design process of the weighting matrices, Q and R, of the LQRIC for the *LC*-HAPF based on Bryson's rule is also given in this paper. Then, the control gain K matrix is calculated through the LQR method by using MATLAB. Finally, the obtained K matrix is applied and the feasibility of LQRC and LQRIC for the *LC*-HAPF are verified by the simulation and experimental results. The results show that LQRC- and LQRIC-controlled *LC*-HAPF can achieve a good compensation performance even under low DC-link voltage. Moreover, the proposed LQRIC shows superior steady-state performance compared with the harmonic compensation, neutral current compensation and reactive power compensation with HCC, PCC and LQRC.

Institutional Review Board Statement: Not applicable.

Informed Consent Statement: Not applicable.

Data Availability Statement: Not applicable.

Conflicts of Interest: The authors declare no conflict of interest.

References

1. Farhoodnea, M.; Mohamed, A.; Shareef, H.; Zayandehroodi, H. Power Quality Impact of Grid-Connected Photovoltaic Generation System in Distribution Networks. In Proceedings of the 2012 IEEE Student Conference on Research and Development (SCOReD), Penang, Malaysia, 5–6 December 2012; pp. 1–6. [CrossRef]
2. Bose, B.K. Power Electronics, Smart Grid, and Renewable Energy Systems. *Proc. IEEE.* **2017**, *105*, 2011–2018. [CrossRef]
3. Di Paolo, M. Analysis of Harmonic Impact of Electric Vehicle Charging on the Electric Power Grid, Based on Smart Grid Regional Demonstration Project—Los Angeles. In Proceedings of the 2017 IEEE Green Energy and Smart Systems Conference (IGESSC), Long Beach, CA, USA, 6–7 November 2017; pp. 1–5. [CrossRef]
4. Anu, G.; Fernandez, F.M. Identification of Harmonic Injection and Distortion Power at Customer Location. In Proceedings of the 2020 19th International Conference on Harmonics and Quality of Power (ICHQP), Dubai, United Arab Emirates, 6–7 July 2020; pp. 1–5. [CrossRef]
5. Subjak, J.S.; McQuilkin, J.S. Harmonics-Causes, Effects, Measurements, and Analysis: An Update. *IEEE Trans. Ind. Appl.* **1990**, *26*, 1034–1042. [CrossRef]
6. Das, J.C. Passive Filters-Potentialities and Limitations. *IEEE Trans. Ind. Appl.* **2004**, *40*, 232–241. [CrossRef]
7. Lascu, C.; Asiminoaei, L.; Boldea, I.; Blaabjerg, F. Frequency Response Analysis of Current Controllers for Selective Harmonic Compensation in Active Power Filters. *IEEE Trans. Ind. Electron.* **2009**, *56*, 337–347. [CrossRef]
8. Lam, C.-S.; Wong, M.-C.; Choi, W.-H.; Cui, X.-X.; Mei, H.-M.; Liu, J.-Z. Design and Performance of an Adaptive Low-DC-Voltage-Controlled *LC*-Hybrid Active Power Filter with a Neutral Inductor in Three-Phase Four-Wire Power Systems. *IEEE Trans. Ind. Electron.* **2014**, *61*, 2635–2647. [CrossRef]
9. Sou, W.-K.; Choi, W.-H.; Chao, C.-W.; Lam, C.-S.; Gong, C.; Wong, C.-K.; Wong, M.-C. A Deadbeat Current Controller of *LC*-Hybrid Active Power Filter for Power Quality Improvement. *IEEE Trans. Emerg.* **2020**, *8*, 3891–3905. [CrossRef]
10. Gong, C.; Sou, W.-K.; Lam, C.-S. Design and Analysis of Vector Proportional–Integral Current Controller for *LC*-Coupling Hybrid Active Power Filter with Minimum DC-Link Voltage. *IEEE Trans. Ind. Electron.* **2021**, *36*, 9041–9056. [CrossRef]
11. Chan, P.-I.; Sou, W.-K.; Lam, C.-S. Improved Model Predictive Control with Signal Correction Technique of *LC*-Coupling Hybrid Active Power Filter. *IEEE Trans. Emerg. Sel. Top. Power Electron.* **2022**, *10*, 4650–4664. [CrossRef]
12. Sou, W.-K.; Chao, C.-W.; Gong, C.; Lam, C.-S.; Wong, C.-K. Analysis, Design, and Implementation of Multi-Quasi-Proportional-Resonant Controller for Thyristor-Controlled *LC*-Coupling Hybrid Active Power Filter (TC*LC*-HAPF). *IEEE Trans. Ind. Electron.* **2022**, *69*, 29–40. [CrossRef]
13. Xiang, Z.; Pang, Y.; Wang, L.; Wong, C.-K.; Lam, C.-S.; Wong, M.-C. Design, Control and Comparative Analysis of an *LCLC* Coupling Hybrid Active Power Filter. *IET Power Electron.* **2020**, *13*, 1207–1217. [CrossRef]
14. Lam, C.-S.; Wong, M.-C.; Han, Y.-D. Hysteresis current control of hybrid active power filters. *IET Power Electron.* **2012**, *5*, 1175–1187. [CrossRef]
15. Ye, T.; Dai, N.; Lam, C.-S.; Wong, M.-C.; Guerrero, J.M. Analysis, Design, and Implementation of a Quasi-Proportional-Resonant Controller for a Multifunctional Capacitive-Coupling Grid-Connected Inverter. *IEEE Trans. Ind Appl.* **2016**, *52*, 4269–4280. [CrossRef]
16. Ahmed, M.; Alsokhiry, F.; Abdel-Khalik, A.S.; Ahmed, K.H.; Al-Turki, Y. Improved Damping Control Method for Grid-Forming Converters Using LQR and Optimally Weighted Feedback Control Loops. *IEEE Access* **2021**, *9*, 87484–87500. [CrossRef]
17. Fan, L.; Liu, P.; Teng, H.; Qiu, G.; Jiang, P. Design of LQR Tracking Controller Combined with Orthogonal Collocation State Planning for Process Optimal Control. *IEEE Access* **2020**, *8*, 223905–223917. [CrossRef]
18. Huerta, F.; Pizarro, D.; Cobreces, S.; Rodriguez, F.J.; Giron, C.; Rodriguez, A. LQG Servo Controller for the Current Control of *LCL* Grid-Connected Voltage-Source Converters. *IEEE Trans. Ind. Electron.* **2012**, *59*, 4272–4284. [CrossRef]
19. Panigrahi, R.; Subudhi, B.; Panda, P.C. A Robust LQG Servo Control Strategy of Shunt-Active Power Filter for Power Quality Enhancement. *IEEE Trans. Power Electron.* **2016**, *31*, 2860–2869. [CrossRef]
20. Ufnalski, B.; Kaszewski, A.; Grzesiak, L.M. Particle Swarm Optimization of the Multioscillatory LQR for a Three-Phase Four-Wire Voltage-Source Inverter with an *LC* Output Filter. *IEEE Trans. Ind. Electron.* **2015**, *62*, 484–493. [CrossRef]
21. De Almeida, P.M.; Ribeiro, A.S.B.; Souza, I.D.N.; de Fernandes, M.C.; Fogli, G.A.; Ćuk, V.; Barbosa, P.G.; Ribeiro, P.F. Systematic Design of a DLQR Applied to Grid-Forming Converters. *IEEE J. Emerg. Sel. Top. Ind. Electron.* **2020**, *1*, 200–210. [CrossRef]
22. Zhang, H.; Feng, T.; Liang, H.; Luo, Y. LQR-Based Optimal Distributed Cooperative Design for Linear Discrete-Time Multiagent Systems. *IEEE Trans. Neural Netw. Learn. Syst.* **2017**, *28*, 599–611. [CrossRef]
23. Gokcek, C.; Kabamba, P.T.; Meerkov, S.M. An LQR/LQG Theory for Systems with Saturating Actuators. *IEEE Trans. Autom. Control* **2001**, *46*, 1529–1542. [CrossRef]
24. Kedjar, B.; Al-Haddad, K. LQR with Integral Action to Enhance Dynamic Performance of Three-Phase Three-Wire Shunt Active Filter. In Proceedings of the 2007 IEEE Power Electronics Specialists Conference, Orlando, FL, USA, 17–21 June 2007; pp. 1138–1144. [CrossRef]

25. Arab, N.; Vahedi, H.; Al-Haddad, K. LQR Control of Single-Phase Grid-Tied PUC5 Inverter with *LCL* Filter. *IEEE Trans. Ind. Electron.* **2020**, *67*, 297–307. [CrossRef]

26. Kedjar, B.; Al-Haddad, K. DSP-Based Implementation of an LQR With Integral Action for a Three-Phase Three-Wire Shunt Active Power Filter. *IEEE Trans. Ind. Electron.* **2009**, *56*, 2821–2828. [CrossRef]

27. Kedjar, B.; Al-Haddad, K. LQ Control of a Three-Phase Four-Wire Shunt Active Power Filter Based on Three-Level NPC Inverter. In Proceedings of the 2008 Canadian Conference on Electrical and Computer Engineering, Niagara Falls, ON, Canada, 6–7 May 2008; pp. 1297–1302. [CrossRef]

28. Santiprapan, P.; Areerak, K.; Areerak, K. Dynamic Model of Active Power Filter in Three-Phase Four-Wire System. In Proceedings of the 2014 11th International Conference on Electrical Engineering/Electronics, Computer, Telecommunications and Information Technology (ECTI-CON), Nakhon, Thailand, 14–17 May 2014; pp. 1–5. [CrossRef]

29. Busatto, T.; Rönnberg, S.; Bollen, M.H.J. Comparison of Models of Single-Phase Diode Bridge Rectifiers for Their Use in Harmonic Studies with Many Devices. *Energies* **2022**, *15*, 66. [CrossRef]

30. Franklin, G.F.; Powell, J.D.; Emami-Naeini, A. *Feedback Control of Dynamic Systems*, 6th ed.; Pearson: Upper Saddle River, NJ, USA, 2010; ISBN 978-0-13-601969-5.

31. *IEEE Std 519-2014 (Revision of IEEE Std 519-1992)*; Recommended Practice and Requirements for Harmonic Control in Electric Power Systems. IEEE: Hoboken, NJ, USA, 2014; pp. 1–29. [CrossRef]